Comput Mech (2008) 42:133–144
DOI 10.1007/s00466-008-0242-x

ORIGINAL PAPER

Geometric nonlinear analysis of plates and cylindrical shells via a linearly conforming radial point interpolation method

X. Zhao · G. R. Liu · K. Y. Dai · Z. H. Zhong · G. Y. Li · X. Han

Received: 28 August 2007 / Accepted: 9 January 2008 / Published online: 30 January 2008

Abstract In this paper, the linearly conforming radial point interpolation method is extended for geometric nonlinear analysis of plates and cylindrical shells. The Sander's nonlinear shell theory is utilized and the arc-length technique is implemented in conjunction with the modified Newton–Raphson method to solve the nonlinear equilibrium equations. The radial and polynomial basis functions are employed to construct the shape functions with Delta function property using a set of arbitrarily distributed nodes in local support domains. Besides the conventional nodal integration, a stabilized conforming nodal integration is applied to restore the conformability and to improve the accuracy of solutions. Small rotations and deformations, as well as finite strains, are assumed for the present formulation. Comparisons of present solutions are made with the results reported in the literature and good agreements are obtained. The numerical examples have demonstrated that the present approach, combined with arc-length method, is quite effective in tracing the load-deflection paths of snap-through and snap-back phenomena in shell problems.

Keywords Shell · Nodal integration · Meshless method · Radial basisfunction · Nonlinear analysis

X. Zhao (✉) · G. R. Liu · K. Y. Dai
Centre for Advanced Computations in Engineering Science (ACES), Department of Mechanical Engineering, The National University of Singapore, 9 Engineering Drive 1, Singapore 117576, Singapore
e-mail: alex.zx69@gmail.com

G. R. Liu
The Singapore-MIT Alliance (SMA),
E4-04-10, 4 Engineering Drive 3, Singapore 117576, Singapore

Z. H. Zhong · G. Y. Li · X. Han
Key Laboratory of Advanced Technology for Vehicle Body Design and Manufacture, M.O.E, Hunan University,
Changsha 410082, People's Republic of China

1 Introduction

Shell structures are often found in engineering structural systems due to peculiarities of their behavior: the curvature of shell structures can be made use to significantly increase their load carrying capacity. The shell analysis, therefore, is of great importance for practical engineering problems. Commonly, the linear analysis is carried out for shells undertaking small displacements under external loads. Nonlinear response of shells, however, should be investigated in the circumstance where shells experience large deformations. Macneal and Harder [1] proposed a standard set of finite element problems for linear analysis of shells. Belytschko et al. [2] investigated the performance of 9-node element in dealing with shear and membrane locking in linear shell analysis. A geometrically exact shell model was reported by Simo et al. [3,4] to study the linear behaviour of shells. For the nonlinear analysis of shells, Sabir and Lock [5] investigated geometrically nonlinear response of cylindrical shells under lateral loading. Bergan and Nygard [6] presented nonlinear shell analysis using the theory of free formulation finite elements. Palazotto and Dennis [7] carried out the nonlinear response of composite shells, and also examined the influence of transverse shear deformation. Recently, Choi and Paik [8] developed a 4-node degenerated shell element for the analysis of shell structures that are undergoing a large deformation. The other works of geometric nonlinear analysis of shells include those given by Sze and Zheng [9], Sze et al. [10], Hauptmann and Schweizerhof [11], Reddy [12] and Arciniega and Reddy [13].

Meshfree methods, which are based on a set of discrete nodes instead of meshes, have been applied in shell analysis by researchers. Krysl and Belytschko [14] presented an element-free Galerkin shell formulation for arbitrary Kirchhoff shells. Noguchi et al. [15] proposed an enhanced

element-free Galerkin method to analyze three-dimensional shell and spatial structures. Li et al. [16] carried out numerical simulations of large deformation of shell structures using meshfree methods.

Radial point interpolation method (RPIM) reported by Wang and Liu [17], a variant of Point interpolation method (PIM) [18], is a meshfree method that employs both polynomial and radial basis functions (RBFs) to construct the shape functions. The RPIM shape functions possess the Kronecker delta function property and the moment matrix is always invertible for arbitrarily scattered nodes due to the adoption of the radial basis function. The RPIM has been successfully applied in many engineering problems, such as simulation of piezoelectric structures [19], three-dimensional elasticity problems [20], and solid mechanics problems [21].

In meshfree methods, Gaussian quadrature is commonly used to evaluate the stiffness matrix. Due to the high computation cost and complexity involved in Gauss integration, nodal integration has been proposed by researchers as an alternative integration approach. The numerical stability and accuracy, however, are not ensured in nodal integration. A variety of efforts has been taken by researchers in order to overcome such shortcomings. Beissel and Belytschko [22] presented a stabilized nodal integration approach for element-free Galerkin method. The spurious near-singular modes in some problems, according to their study, were successfully eliminated. But for problems without unstable modes, the accuracy of solutions deteriorated. Bonet and Kulasegaram [23] proposed a correction procedure to improve the accuracy of nodal integration by avoiding the computation of a second-order derivative of shape functions. A stabilized conforming nodal integration for the Galerkin meshfree method was presented by Chen et al. [24] to achieve higher efficiency with desired accuracy and convergent properties. An integration constraint (IC) was introduced as a necessary condition for a linear exactness in the meshfree Galerkin approximation. The Gauss integration has been demonstrated to violate IC and produces prominent errors.

In this paper, geometric nonlinear analysis of plates and shells is studied via a linearly conforming radial point interpolation method (LC-RPIM). The nonlinear shell theory employed in present formulation only takes into account the nonlinear membrane strain, while the bending and shear parts are still linear. Furthermore, it is should be noted that small rotations and deformations, as well as finite strains, are assumed for the present formulation. The conventional nodal integration is used to evaluate the membrane and shear stiffness terms, while a stabilized nodal integration technique is employed to estimate the bending stiffness term in order to achieve conformity, higher accuracy and efficiency. The load-deflection responses for present cases are determined by using arc-length approach [25]. The numerical examples show that present method not only avoids membrane and shear locking, but also provides good accuracy, efficiency and stability in capturing the snap-through and snap-back phenomena in shell problems.

2 Radial point interpolation method

In this section, a brief introduction of the construction of RPIM shape functions is given. Consider an approximation of function $u(\mathbf{x})$ in a support domain with a set of arbitrarily scattered points at $\mathbf{x}_i$, $(i = 1, 2, \ldots, n)$, where n is the number of nodes in the support domain. The approximation function $u(\mathbf{x})$ can be expressed in the form of

$$u(\mathbf{x}) = \sum_{i=1}^{n} r_i(\mathbf{x}) a_i + \sum_{j=1}^{m} p_j(\mathbf{x}) b_j = \mathbf{r}^{\mathrm{T}}(\mathbf{x})\mathbf{a} + \mathbf{p}^{\mathrm{T}}(\mathbf{x})\mathbf{b} \quad (1)$$

where a_i is the unknown coefficient for the radial basis function $r_i(\mathbf{x})$, which is defined as

$$r_i(x, y) = \left[(x - x_i)^2 + (y - y_i)^2 + R_c^2\right]^q \quad (2)$$

where q and R_c are two optimal shape parameters, which had been generalized as an arbitrary real number and examined in detail by Wang and Liu [17]. b_j is the coefficient for polynomial basis $p_j(\mathbf{x})$, and m is determined according to the polynomial basis selected. For example, a quadratic basis in two-dimension requires $m = 6$, which is chosen in this study. The polynomial basis is given by

$$\mathbf{p}^{\mathrm{T}}(\mathbf{x}) = \left[1, x, y, x^2, xy, y^2\right] \quad (3)$$

The coefficients a_i and b_j in Eq. (1) are determined by satisfying the reproducing condition at the nodes in the support domain. The interpolation at the kth node is expressed as

$$u_k = u(\mathbf{x}_k) = \sum_{i=1}^{n} a_i r_i(\mathbf{x}_k) + \sum_{j=1}^{m} b_j p_j(\mathbf{x}_k), \quad k = 1,\ 2, \ldots,\ n \quad (4)$$

In order to solve coefficients a_i and b_j uniquely, the following constraints need to be imposed

$$\sum_{i=1}^{n} p_j(\mathbf{x}_k) a_i = 0, \quad j = 1, 2, \ldots, m \quad (5)$$

Equation (5) can be expressed in matrix form as

$$\mathbf{G}\begin{Bmatrix}\mathbf{a}\\ \mathbf{b}\end{Bmatrix} = \begin{Bmatrix}\mathbf{u}^e\\ \mathbf{0}\end{Bmatrix} \quad (6)$$

where matrix $\mathbf{G}$ and nodal displacement vector $\mathbf{u}^e$ are given respectively as

$$\mathbf{G} = \begin{bmatrix}\mathbf{R}_0 & \mathbf{P}_0\\ \mathbf{P}_0^{\mathrm{T}} & \mathbf{0}\end{bmatrix}, \quad \mathbf{u}^e = [u_1, u_2, u_3, \ldots, u_n]^{\mathrm{T}} \quad (7)$$

The moment matrix $\mathbf{R}_0$ is defined as

$$\mathbf{R}_0 = \begin{bmatrix} r_1(x_1, y_1) & r_2(x_1, y_1) & \cdots & r_n(x_1, y_1) \\ r_1(x_2, y_2) & r_2(x_2, y_2) & \cdots & r_n(x_2, y_2) \\ \vdots & \vdots & \vdots & \vdots \\ r_1(x_n, y_n) & r_2(x_n, y_n) & \cdots & r_n(x_n, y_n) \end{bmatrix} \tag{8}$$

and $\mathbf{P}_0$ is expressed as

$$\mathbf{P}_0 = \begin{bmatrix} p_1(x_1, y_1) & p_2(x_1, y_1) & \cdots & p_m(x_1, y_1) \\ p_1(x_2, y_2) & p_2(x_2, y_2) & \cdots & p_m(x_2, y_2) \\ \vdots & \vdots & \vdots & \vdots \\ p_1(x_n, y_n) & p_2(x_n, y_n) & \cdots & p_m(x_n, y_n) \end{bmatrix} \tag{9}$$

Solving Eq. (6) yields

$$\begin{Bmatrix} \mathbf{a} \\ \mathbf{b} \end{Bmatrix} = \mathbf{G}^{-1} \begin{Bmatrix} \mathbf{u}^e \\ \mathbf{0} \end{Bmatrix}. \tag{10}$$

The approximation of function $u(\mathbf{x})$ is finally expressed as

$$\mathbf{u}(\mathbf{x}) = \begin{bmatrix} \mathbf{R}_0^{\mathrm{T}}(\mathbf{x}) & \mathbf{P}_0^{\mathrm{T}}(\mathbf{x}) \end{bmatrix} \mathbf{G}^{-1} \begin{Bmatrix} \mathbf{u}^e \\ \mathbf{0} \end{Bmatrix} = \boldsymbol{\varphi}(\mathbf{x})\mathbf{u}^e \tag{11}$$

where $\boldsymbol{\varphi}(\mathbf{x})$ is the matrix of the shape functions and is given by

$$\begin{aligned} \boldsymbol{\varphi}(\mathbf{x}) &= \begin{bmatrix} \phi_1(\mathbf{x}) & \phi_2(\mathbf{x}) & \cdots & \phi_n(\mathbf{x}) \end{bmatrix} \\ \phi_k(\mathbf{x}) &= \sum_{i=1}^{n} r_i(\mathbf{x})\bar{G}_{i,k} + \sum_{j=1}^{m} p_j(\mathbf{x})\bar{G}_{n+j,k} \end{aligned} \tag{12}$$

where $\bar{G}_{i,k}$ is the element of matrix $\mathbf{G}^{-1}$.

It should be noticed that the present shape functions possess the reproducing properties due to the addition of polynomial basis, satisfy the Delta function properties and unity partition property, and always exist because of the adoption of RBFs. Therefore, the completeness and reproducing conditions are satisfied, the convergence of present method is ensured.

3 Strain smoothing technique

It has been demonstrated by Chen et al. [24] that, to ensure linear exactness in Galerkin approximation, integration constraints (IC) need to be satisfied in domain integration. In order to remove the instability in direct nodal integration, a stabilized conforming nodal integration that meets integration constraints is introduced [24]. Recently, Sze et al. [26] discussed, from a domain decomposition point of view, how stabilized conforming nodal integration guarantees linear exactness and eradicates spurious oscillation in direct nodal integration. They also demonstrated that stabilized conforming nodal integration can be formulated by the Hellinger–Reissner Principle and thus justified in the classical variational sense.

The stabilized conforming nodal integration is based on a stain smoothing technique. Consider a domain Ω discretized by a set of nodes, Ω_L denotes the representative domain of a node $\mathbf{x}_L$. The strain smoothing at the node $\mathbf{x}_L$ is defined as

$$\tilde{\varepsilon}_{ij}(\mathbf{x}_L) = \int_{\Omega} \varepsilon_{ij}(\mathbf{x})\Phi(\mathbf{x}; \mathbf{x} - \mathbf{x}_L)d\Omega \tag{13}$$

where ε_{ij} is the strain and Φ is a smoothing function. A constant smoothing function is given by

$$\Phi(\mathbf{x}; \mathbf{x} - \mathbf{x}_L) = \begin{cases} 1/A_L & \mathbf{x} \in \Omega_L \\ 0 & \mathbf{x} \notin \Omega_L \end{cases} \tag{14}$$

in which $A_L = \int_{\Omega_L} d\Omega$ is the area of the representative domain of node L, which is generated either from the Voronoi diagram or Delaunay triangulation shown in Fig. 1. Applying the divergence theorem to Eq. (13) yields the following strain smoothing expression

$$\tilde{\varepsilon}_{ij}(\mathbf{x}_L) = \frac{1}{2A_L} \int_{\Gamma_L} (u_i^h n_j + u_j^h n_i)d\Gamma \tag{15}$$

where Γ_L is the boundary of the representative domain of node L and $\mathbf{n}$ is the outward normal of boundary Γ_L as shown in Fig. 2. For a two-dimensional problem, introducing RPIM shape functions into Eq. (15) yields

$$\tilde{\boldsymbol{\varepsilon}}^h(\mathbf{x}_L) = \sum_{I \in S_L} \tilde{\mathbf{B}}_I(\mathbf{x}_L)\mathbf{u}_I \tag{16}$$

$$\tilde{\mathbf{B}}_I(\mathbf{x}_L) = \begin{bmatrix} \tilde{b}_{I1}(\mathbf{x}_L) & 0 \\ 0 & \tilde{b}_{I2}(\mathbf{x}_L) \\ \tilde{b}_{I2}(\mathbf{x}_L) & \tilde{b}_{I1}(\mathbf{x}_L) \end{bmatrix} \tag{17}$$

$$\tilde{b}_{Ii}(\mathbf{x}_L) = \frac{1}{A_L} \int_{\Gamma_L} \phi_I(\mathbf{x}_L)n_i(\mathbf{x}_L)d\Gamma \quad (i = 1,\ 2) \tag{18}$$

where S_L is a group of nodes whose shape function supports cover node L. It has been demonstrated [24] that the smoothing gradient Eq. (17) satisfies the integration constraints in nodal integration.

4 Formulation

4.1 Energy functional

A cylindrical shell panel is shown in Fig. 3, where a coordinate system (x, y, z) is fixed on the middle surface of the panel. This panel is of a length L, radius R, span angle θ_0, and thickness h. According to the first order shear deformation

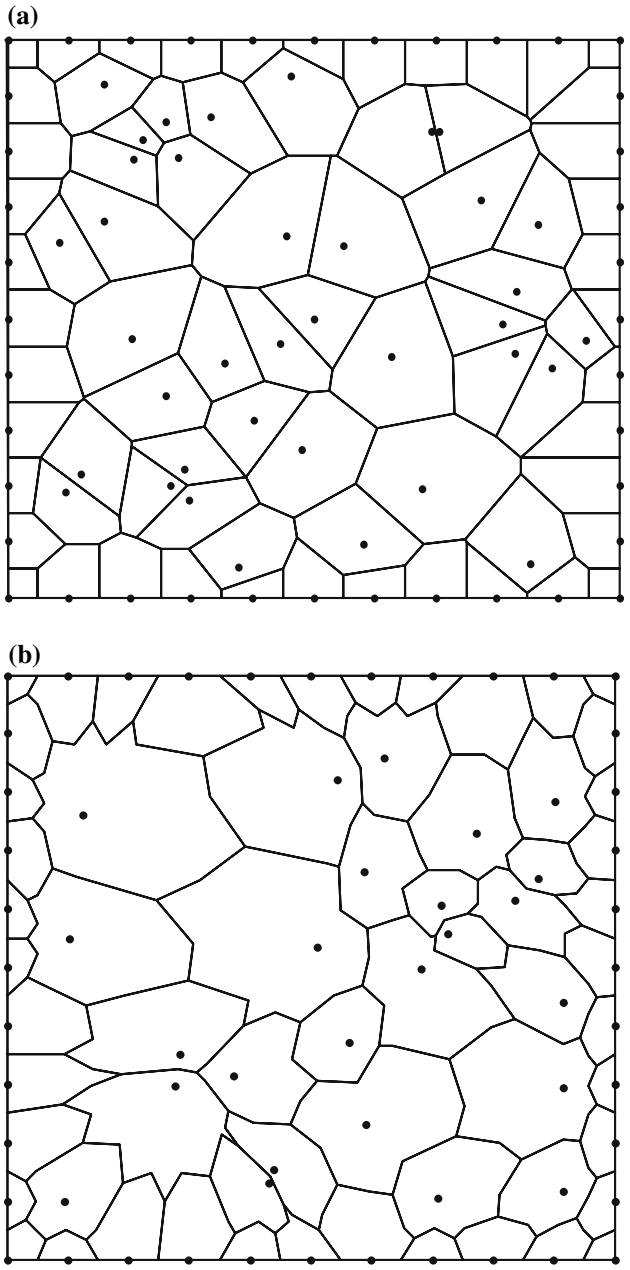

Fig. 1 Problem domain represented by irregular nodes. **a** Voronoi diagram. **b** Nodal domain by Delaunay triangulation

shell theory, the displacement field is expressed as

$$\begin{aligned} u(x, y, z) &= u_0(x, y) + z\psi_x(x, y) \\ v(x, y, z) &= v_0(x, y) + z\psi_y(x, y) \\ w(x, y, z) &= w_0(x, y) \end{aligned} \tag{19}$$

where u_0, v_0 and w_0 denote the displacements of the mid-surface of the shell in the x, y, and z directions, ψ_x and ψ_y are the rotations of the transverse normal about the y and x axes, respectively.

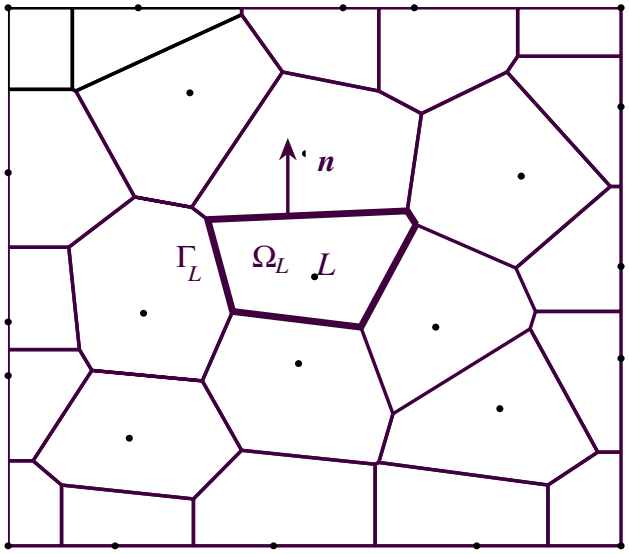

Fig. 2 A nodal representative domain

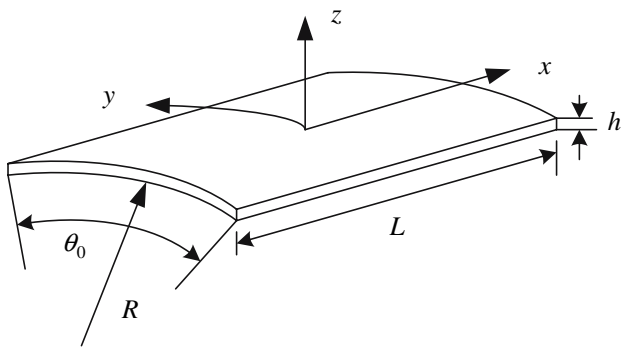

Fig. 3 Geometry of a cylindrical shell panel

A modified nonlinear strain-displacement equations [12] of the Sanders nonlinear shell theory [27] is expressed as

$$\left\{ \begin{matrix} \varepsilon_{xx} \\ \varepsilon_{yy} \\ \gamma_{xy} \end{matrix} \right\} = \boldsymbol{\varepsilon}_0 + z\kappa, \quad \left\{ \begin{matrix} \gamma_{yz} \\ \gamma_{xz} \end{matrix} \right\} = \boldsymbol{\gamma}_0 \tag{20}$$

where

$$\boldsymbol{\varepsilon}_0 = \boldsymbol{\varepsilon}_{0L} + \boldsymbol{\varepsilon}_{0N} \tag{21}$$

$$\boldsymbol{\varepsilon}_{0L} = \left\{ \begin{matrix} \frac{\partial u_0}{\partial x} \\ \frac{\partial v_0}{\partial y} \\ \frac{\partial u_0}{\partial y} + \frac{\partial v_0}{\partial x} \end{matrix} \right\}, \quad \boldsymbol{\varepsilon}_{0N} = \left\{ \begin{matrix} \frac{1}{2}\left(\frac{\partial w_0}{\partial x}\right)^2 \\ \frac{1}{2}\left(\frac{\partial w_0}{\partial y}\right)^2 \\ \frac{\partial w_0}{\partial x}\frac{\partial w_0}{\partial y} \end{matrix} \right\},$$

$$\kappa = \left\{ \begin{matrix} \frac{\partial \psi_x}{\partial x} \\ \frac{\partial \psi_y}{\partial y} \\ \frac{\partial \psi_x}{\partial y} + \frac{\partial \psi_y}{\partial x} \end{matrix} \right\}, \quad \boldsymbol{\gamma}_0 = \left\{ \begin{matrix} \psi_y + \frac{\partial w_0}{\partial y} - \frac{v_0}{R} \\ \psi_x + \frac{\partial w_0}{\partial x} \end{matrix} \right\} \tag{22}$$

The stress resultants are given by

$$\begin{Bmatrix} \bar{\mathbf{N}} \\ \bar{\mathbf{M}} \\ \bar{\mathbf{Q}} \end{Bmatrix} = \begin{bmatrix} \bar{\mathbf{A}} & \bar{\mathbf{B}} & \mathbf{0} \\ \bar{\mathbf{B}} & \bar{\mathbf{D}} & \mathbf{0} \\ \mathbf{0} & \mathbf{0} & \bar{\mathbf{A}}_s \end{bmatrix} \begin{Bmatrix} \boldsymbol{\varepsilon}_0 \\ \kappa \\ \boldsymbol{\gamma}_0 \end{Bmatrix} \tag{23}$$

where $\bar{\mathbf{N}}$, $\bar{\mathbf{M}}$ and $\bar{\mathbf{Q}}$ denote in-plane force resultants, moment resultants and the shear force resultants respectively, and are expressed as

$$\bar{\mathbf{N}} = \begin{Bmatrix} N_{xx} \\ N_{yy} \\ N_{xy} \end{Bmatrix}, \quad \bar{M} = \begin{Bmatrix} M_{xx} \\ M_{yy} \\ M_{xy} \end{Bmatrix}, \quad \bar{\mathbf{Q}} = \begin{Bmatrix} Q_y \\ Q_x \end{Bmatrix} \tag{24}$$

$\bar{\mathbf{A}}$, $\bar{\mathbf{D}}$, $\bar{\mathbf{B}}$ and $\bar{\mathbf{A}}_s$ represent matrices of extensional stiffnesses, bending stiffnesses, bending-extensional coupling stiffnesses and transverse shear stiffnesses, and are defined as

$$\bar{\mathbf{A}} = \begin{bmatrix} A_{11} & A_{12} & A_{16} \\ A_{12} & A_{22} & A_{26} \\ A_{16} & A_{26} & A_{66} \end{bmatrix}, \quad \bar{\mathbf{B}} = \begin{bmatrix} B_{11} & B_{12} & B_{16} \\ B_{12} & B_{22} & B_{26} \\ B_{16} & B_{26} & B_{66} \end{bmatrix},$$

$$\bar{\mathbf{D}} = \begin{bmatrix} D_{11} & D_{12} & D_{16} \\ D_{12} & D_{22} & D_{26} \\ D_{16} & D_{26} & D_{66} \end{bmatrix}, \quad \bar{\mathbf{A}}_\mathbf{s} = \begin{bmatrix} A_{44} & A_{45} \\ A_{45} & A_{55} \end{bmatrix}$$

$$(A_{ij}, B_{ij}, D_{ij}) = \int_{-h/2}^{h/2} Q_{ij}(1, z, z^2)dz,$$

$$A_{sij} = \int_{-h/2}^{h/2} K Q_{ij} dz \tag{25}$$

The stiffnesses A_{ij}, B_{ij}, and D_{ij} are defined for $i, j = 1, 2, 6$, respectively, whereas A_{sij} is defined for $i, j = 4, 5$. K denotes the transverse shear correction coefficient and $K = 5/6$ is taken in this study. Q_{ij} stands for the engineering constant, which is defined as

$$Q_{11} = \frac{E_{11}}{1 - \nu_{12}\nu_{21}}, \quad Q_{12} = \frac{\nu_{12}E_{22}}{1 - \nu_{12}\nu_{21}},$$
$$Q_{22} = \frac{E_{22}}{1 - \nu_{12}\nu_{21}} \tag{26}$$
$$Q_{66} = G_{12}, \quad Q_{44} = G_{23}, \quad Q_{55} = G_{13}$$

where E_{11} and E_{22} are the elastic moduli in the principle material coordinates; G_{12}, G_{13}, and G_{23} are the shear moduli; and ν_{12} and ν_{21} are the Poisson's ratios. For a shell composed of different layers of materials, the corresponding stiffnesses in Eq. (25) can be obtained according to transformation law [12].

The strain energy of the panel is expressed by

$$U_\varepsilon = \frac{1}{2}\int_\Omega \boldsymbol{\varepsilon}^\mathrm{T}\mathbf{S}\boldsymbol{\varepsilon} d\Omega \tag{27}$$

where $\boldsymbol{\varepsilon}$ and $\mathbf{S}$ are given by

$$\boldsymbol{\varepsilon} = \begin{Bmatrix} \boldsymbol{\varepsilon}_0 \\ \kappa \\ \boldsymbol{\gamma}_0 \end{Bmatrix} \tag{28}$$

$$\mathbf{S} = \begin{bmatrix} \bar{\mathbf{A}} & \bar{\mathbf{B}} & \mathbf{0} \\ \bar{\mathbf{B}} & \bar{\mathbf{D}} & \mathbf{0} \\ \mathbf{0} & \mathbf{0} & \bar{\mathbf{A}}_s \end{bmatrix} = \begin{bmatrix} \hat{\mathbf{D}} & \mathbf{0} \\ \mathbf{0} & \bar{\mathbf{A}}_s \end{bmatrix} \tag{29}$$

The external work done due to surface traction and body force is given by

$$W_\mathrm{e} = \int_\Omega \mathbf{u}^\mathrm{T}\bar{\mathbf{f}} d\Omega + \int_\Gamma \mathbf{u}^\mathrm{T}\bar{\mathbf{t}} d\Gamma \tag{30}$$

where $\bar{\mathbf{f}}$ and $\bar{\mathbf{t}}$ represent the external load and prescribed traction on the natural boundary, respectively.

The total potential energy functional for the panel is expressed as

$$\Pi_s = U_\varepsilon - W_\mathrm{e} \tag{31}$$

4.2 Nodal integration

The discrete nodes are generated freely on the $x - y$ space in the parametric coordinate system. The nodal representative domains based on Delaunay triangulation are obtained on the $x - y$ space. For a shell panel domain Ω discretized by a set of nodes x_I, $I = 1, \ldots, NP$, the approximations of displacements and rotations of the mid-plane of the panel are expressed using RPIM shape functions as

$$\mathbf{u}_0^h = \begin{pmatrix} u_0^h \\ v_0^h \\ w_0^h \\ \psi_x^h \\ \psi_y^h \end{pmatrix} = \sum_{I=1}^{NP} \phi_I \begin{pmatrix} u_I \\ v_I \\ w_I \\ \psi_{xI} \\ \psi_{yI} \end{pmatrix} = \sum_{I=1}^{NP} \phi_I(\mathbf{x})\mathbf{u}_I \tag{32}$$

Substituting Eq. (32) into Eq. (31) and taking variation to the energy functional yield the equilibrium equation

$$\mathbf{K}_\mathrm{s}(\mathbf{u})\mathbf{u} = \mathbf{F} \tag{33}$$

where the secant stiffness matrix $\mathbf{K}_\mathrm{s}$ is defined as

$$\mathbf{K}_\mathrm{s}(\mathbf{u}) = \mathbf{K}^L + \mathbf{K}^{NL}(\mathbf{u}) \tag{34}$$

in which $\mathbf{K}^L$ represents the linear stiffness matrix and $\mathbf{K}^{NL}$ denotes the nonlinear stiffness matrix, which is a function of displacements.

The matrices $\mathbf{K}^L$, $\mathbf{K}^{NL}$, $\mathbf{u}$ and $\mathbf{F}$ are given by

$$\mathbf{K}^L = \mathbf{K}^b + \mathbf{K}^m + \mathbf{K}^{sh} \tag{35}$$

$$\mathbf{u} = \begin{bmatrix} \mathbf{u}_1 & \mathbf{u}_2 & \cdots & \mathbf{u}_n \end{bmatrix}^\mathrm{T} \tag{36}$$

where

$$\mathbf{K}_{IJ}^{b} = \int_{\Omega} \mathbf{B}_I^{b^{\mathrm{T}}} \bar{\mathbf{D}} \mathbf{B}_J^{b} d\Omega \tag{37}$$

$$\mathbf{K}_{IJ}^{m} = \int_{\Omega} \mathbf{B}_I^{m^{\mathrm{T}}} \bar{\mathbf{A}} \mathbf{B}_J^{m} d\Omega + \int_{\Omega} \mathbf{B}_I^{m^{\mathrm{T}}} \bar{\mathbf{B}} \mathbf{B}_J^{b} d\Omega + \int_{\Omega} \mathbf{B}_I^{b^{\mathrm{T}}} \bar{\mathbf{B}} \mathbf{B}_J^{m} d\Omega \tag{38}$$

$$\mathbf{K}_{IJ}^{NL} = \int_{\Omega} \left(\frac{1}{2} \mathbf{B}_I^{L^{\mathrm{T}}} \mathbf{S} \mathbf{B}_J^{NL} + \mathbf{B}_I^{NL^{\mathrm{T}}} \mathbf{S} \mathbf{B}_J^{L} + \frac{1}{2} \mathbf{B}_I^{NL^{\mathrm{T}}} \mathbf{S} \mathbf{B}_J^{NL} \right) d\Omega \tag{39}$$

$$\mathbf{K}_{IJ}^{\mathrm{sh}} = \int_{\Omega} \mathbf{B}_I^{s^{\mathrm{T}}} \bar{\mathbf{A}}_s \mathbf{B}_J^{s} d\Omega \tag{40}$$

$$\mathbf{F}_I = \int_{\Omega} \phi_I \bar{\mathbf{f}} d\Omega + \int_{\Gamma} \phi_I \bar{\mathbf{t}} d\Gamma \tag{41}$$

$$\mathbf{B}_I^{L} = \begin{bmatrix} \mathbf{B}_I^{m} \\ \mathbf{B}_I^{b} \\ \mathbf{B}_I^{s} \end{bmatrix}, \quad \mathbf{B}_I^{NL} = \overline{\mathbf{H}} \overline{\mathbf{G}} \tag{42}$$

The stiffness matrix in Eq. (37) is evaluated using the stabilized nodal integration technique introduced in Sect. 3, while Eqs. (38) to (41) are computed by the direct nodal integration. The approximations of Eqs. (37) to (41) are given as follows

$$\mathbf{K}_{IJ}^{b} = \sum_{L=1}^{NP} \tilde{\mathbf{B}}_I^{b^{\mathrm{T}}}(\mathbf{x}_L) \bar{\mathbf{D}} \tilde{\mathbf{B}}_J^{b}(\mathbf{x}_L) A_L,$$

$$\mathbf{K}_{IJ}^{\mathrm{sh}} = \sum_{L=1}^{NP} \mathbf{B}_I^{s^{\mathrm{T}}}(\mathbf{x}_L) \bar{\mathbf{A}}_s \mathbf{B}_J^{s}(\mathbf{x}_L) A_L \tag{43}$$

$$\mathbf{K}_{IJ}^{m} = \sum_{L=1}^{NP} \left[\mathbf{B}_I^{m^{\mathrm{T}}}(\mathbf{x}_L) \bar{\mathbf{A}} \mathbf{B}_J^{m}(\mathbf{x}_L) + \mathbf{B}_I^{m^{\mathrm{T}}}(\mathbf{x}_L) \bar{\mathbf{B}} \mathbf{B}_J^{b}(\mathbf{x}_L) + \mathbf{B}_I^{b^{\mathrm{T}}}(\mathbf{x}_L) \bar{\mathbf{B}} \mathbf{B}_J^{m}(\mathbf{x}_L) \right] A_L \tag{44}$$

$$\mathbf{K}_{IJ}^{NL} = \sum_{L=1}^{NP} \left[\frac{1}{2} \mathbf{B}_I^{L^{\mathrm{T}}}(\mathbf{x}_L) \mathbf{S} \mathbf{B}_J^{L}(\mathbf{x}_L) + \mathbf{B}_I^{NL^{\mathrm{T}}}(\mathbf{x}_L) \mathbf{S} \mathbf{B}_J^{L}(\mathbf{x}_L) + \frac{1}{2} \mathbf{B}_I^{NL^{\mathrm{T}}}(\mathbf{x}_L) \mathbf{S} \mathbf{B}_J^{NL}(\mathbf{x}_L) \right] A_L \tag{45}$$

$$\mathbf{F}_I = \sum_{L=1}^{NP} \phi_I(\mathbf{x}_L) \mathbf{f}(\mathbf{x}_L) A_L + \sum_{L=1}^{\mathrm{NPb}} \phi_I(\mathbf{x}_L) \bar{\mathbf{t}}(\mathbf{x}_L) s_L \tag{46}$$

where $\mathbf{x}_L$ and A_L are node coordinate and the nodal representative area, respectively, *NPb* is the number of nodes on the natural boundary, and s_L are the weights associated with the boundary point obtained from Delaunay triangulation. $\tilde{\mathbf{B}}_I^{b}(\mathbf{x}_L)$, $\mathbf{B}_I^{b}(\mathbf{x}_L)$, $\mathbf{B}_I^{m}(\mathbf{x}_L)$, $\mathbf{B}_I^{s}(\mathbf{x}_L)$, $\bar{\mathbf{H}}$ and $\bar{\mathbf{G}}$ are given by

$$\tilde{\mathbf{B}}_I^{b}(\mathbf{x}_L) = \begin{bmatrix} 0 & 0 & 0 & \tilde{b}_{Ix}(\mathbf{x}_L) & 0 \\ 0 & 0 & 0 & 0 & \tilde{b}_{Iy}(\mathbf{x}_L) \\ 0 & 0 & 0 & \tilde{b}_{Iy}(\mathbf{x}_L) & \tilde{b}_{Ix}(\mathbf{x}_L) \end{bmatrix} \tag{47}$$

$$\mathbf{B}_I^{b}(\mathbf{x}_L) = \begin{bmatrix} 0 & 0 & 0 & \frac{\partial \phi_I(\mathbf{x}_L)}{\partial x} & 0 \\ 0 & 0 & 0 & 0 & \frac{\partial \phi_I(\mathbf{x}_L)}{\partial y} \\ 0 & 0 & 0 & \frac{\partial \phi_I(\mathbf{x}_L)}{\partial y} & \frac{\partial \phi_I(\mathbf{x}_L)}{\partial x} \end{bmatrix} \tag{48}$$

$$\tilde{b}_{Ix}(\mathbf{x}_L) = \frac{1}{A_L} \int_{\Gamma_L} \phi_I(\mathbf{x}) n_x(\mathbf{x}) d\Gamma,$$

$$\tilde{b}_{Iy}(\mathbf{x}_L) = \frac{1}{A_L} \int_{\Gamma_L} \phi_I(\mathbf{x}) n_y(\mathbf{x}) d\Gamma \tag{49}$$

$$\mathbf{B}_I^{m}(\mathbf{x}_L) = \begin{bmatrix} \frac{\partial \phi_I(\mathbf{x}_L)}{\partial x} & 0 & 0 & 0 & 0 \\ & \frac{\partial \phi_I(\mathbf{x}_L)}{\partial y} & \frac{\phi_I(\mathbf{x}_L)}{R} & 0 & 0 \\ \frac{\partial \phi_I(\mathbf{x}_L)}{\partial y} & \frac{\partial \phi_I(\mathbf{x}_L)}{\partial x} & 0 & 0 & 0 \end{bmatrix} \tag{50}$$

$$\mathbf{B}_I^{s}(\mathbf{x}_L) = \begin{bmatrix} 0 & 0 & \frac{\partial \phi_I(\mathbf{x}_L)}{\partial x} & \phi_I(\mathbf{x}_L) & 0 \\ 0 & -\frac{\phi_I(\mathbf{x}_L)}{R} & \frac{\partial \phi_I(\mathbf{x}_L)}{\partial y} & 0 & \phi_I(\mathbf{x}_L) \end{bmatrix} \tag{51}$$

$$\bar{\mathbf{H}} = \begin{bmatrix} \frac{\partial w}{\partial x} & 0 & \frac{\partial w}{\partial y} & 0 & 0 & 0 & 0 & 0 \\ 0 & \frac{\partial w}{\partial y} & \frac{\partial w}{\partial x} & 0 & 0 & 0 & 0 & 0 \end{bmatrix}^{\mathrm{T}} \tag{52}$$

$$\bar{\mathbf{G}} = \begin{bmatrix} 0 & 0 & \frac{\partial \phi_I(\mathbf{x}_L)}{\partial x} & 0 & 0 \\ 0 & 0 & \frac{\partial \phi_I(\mathbf{x}_L)}{\partial y} & 0 & 0 \end{bmatrix} \tag{53}$$

In order to solve the nonlinear equation system Eq. (33), an iterative algorithm, either Newton–Raphson method or modified Newton–Raphson method, is typically used. An incremental form of Eq. (33), required by the Newton-type methods, should be provided. Equation (33) is rearranged as

$$\mathbf{g}(\mathbf{u}) = \mathbf{K}_s(\mathbf{u})\mathbf{u} - \mathbf{F} = 0 \tag{54}$$

The external load is assumed to be proportional to a fixed load $\mathbf{F}_0$ as

$$\mathbf{F} = \lambda \mathbf{F}_0 \tag{55}$$

where λ is a load level scaling factor. The nonlinear equilibrium equation (54) is rewritten as

$$\mathbf{g}(\mathbf{u}, \lambda) = \mathbf{K}_s(\mathbf{u})\mathbf{u} - \lambda \mathbf{F}_0 \tag{56}$$

For a new equilibrium state, the following conditions should be hold

$$\mathbf{g}(\mathbf{u} + \Delta\mathbf{u}, \lambda + \Delta\lambda) = 0 \tag{57}$$

In which $\Delta\mathbf{u}$ represents the increment displacement, and $\Delta\lambda$ denotes the increment load factor. Applying Taylor series expansion to Eq. (57) yields the following incremental form of the equation

$$\mathbf{K}_t \Delta\mathbf{u} = \Delta\lambda \mathbf{F}_0 - \mathbf{g}(\mathbf{u}, \lambda) \tag{58}$$

where $\mathbf{K}_t$ is tangent stiffness matrix and expressed as

$$\mathbf{K}_t = \mathbf{K}^L + \mathbf{K}^N + \mathbf{K}^G \tag{59}$$

in which $\mathbf{K}^L$ is the linear stiffness matrix given in Eq. (35), $\mathbf{K}^N$ represents the nonlinear stiffness matrix related to displacements and is given by

$$\mathbf{K}_{IJ}^N = \int_\Omega \left(\mathbf{B}_I^{L^{\mathrm{T}}} \mathbf{S} \mathbf{B}_J^{NL} + \mathbf{B}_I^{NL^{\mathrm{T}}} \mathbf{S} \mathbf{B}_J^{L} + \mathbf{B}_I^{NL^{\mathrm{T}}} \mathbf{S} \mathbf{B}_J^{NL} \right) d\Omega \tag{60}$$

$\mathbf{K}^G$ denotes the geometric stiffness matrix and is described as

$$\mathbf{K}_{IJ}^G = \int_\Omega \bar{\mathbf{G}}_I^{\mathrm{T}} \hat{\mathbf{N}} \bar{\mathbf{G}}_J d\Omega \tag{61}$$

where $\bar{\mathbf{G}}$ is given in Eq. (53) and stress matrix $\hat{\mathbf{N}}$ is defined as

$$\hat{\mathbf{N}} = \begin{bmatrix} N_{xx} & N_{xy} \\ N_{xy} & N_{yy} \end{bmatrix} \tag{62}$$

In the incremental-iterative method, each load step includes the application of external load and subsequent iterations to restore equilibrium. In this paper, the subscript i is used to denote the load step number, and superscript j is chosen to represent the iteration cycle.Iterative cycles start at $j = 1$, which corresponds to the external load increment of every load step i. The equilibrium iteration commences at $j = 2$. The generalized equation for the incremental-iterative process is given by

$$\begin{aligned} [\mathbf{K}_t]_i \, \Delta \mathbf{u}_i^j &= \Delta \lambda_i^j \mathbf{F}_0 - \mathbf{g}_i^{j-1} \\ &= \Delta \lambda_i^j \mathbf{F}_0 - \left[\mathbf{K}_s(\mathbf{u}_i^{j-1}) \mathbf{u}_i - \lambda_i^{j-1} \mathbf{F}_0 \right] \end{aligned} \tag{63}$$

The displacement increment $\Delta \mathbf{u}_i^j$ is written as the combination of two parts, one is from external load increment and the other stems from the residual force,

$$\begin{aligned} \Delta \mathbf{u}_i^j &= \left[(\mathbf{K}_t)_i \right]^{-1} \left\{ \Delta \lambda_i^j \mathbf{F}_0 - \left[\mathbf{K}_s(\mathbf{u}_i^{j-1}) \mathbf{u}_i - \lambda_i^{j-1} \mathbf{F}_0 \right] \right\} \\ &= \Delta \lambda_i^j \left[\mathbf{u}_f \right]_i + \left[\Delta \mathbf{u}_R \right]_i^j \end{aligned} \tag{64}$$

In this paper, the tangent stiffness matrix is only computed at the beginning of each load step and is then held constant throughout the iterative cycles. The arc-length iterative strategy is utilized to determine the load increment. The convergence criterion is given by

$$\frac{\|\mathbf{g}(\mathbf{u}, \lambda)\|}{\|\mathbf{F}(\mathbf{u}, \lambda)\|} < \zeta \tag{65}$$

The tolerance for convergence constant ζ is set to 0.001 in this study.

5 Numerical examples

In this section, numerical examples for nonlinear analysis of plates and shells are presented to demonstrate the performance of the present method. The displacement shape functions are constructed using radial point interpolation method. The shape parameters q and R_c are taken as 1.03 and 1.42, respectively [17]. The scaling factor of support domain of 3.4 is used. The shear correction coefficient $K = 5/6$ is adopted. The convergence tolerance $\zeta = 0.1\%$ is set. The nodes are regularly distributed, and the nodal integration domain is generated via Delaunay triangulation. Trapezoidal rule with two-point on each segment for integration is utilized. The smoothing technique is applied in evaluating the bending stiffness, while the membrane and shear terms are estimated by direct nodal integration method. The nonlinear equilibrium equation system is solved by using the arc-length method to obtain the full load-deflection paths involving limit points with both snap-through and snap-back phenomena.

5.1 Convergence studies

Convergence studies are performed based on the nodal distributions of a simply supported plate ($a/h = 10$) and a clamped plate ($a/h = 100$), which are subjected to transverse uniform load, as shown in Fig. 4. The Poisson ratio of the plates is $\nu = 0.3$. Table 1 shows the variation of nondimentional center deflection $\tilde{w} = w_0 E h^3 / q_0 a^4$ with nodal distributions. It is seen that a relatively stable convergent trend is observed for both the simply supported and clamped plates.

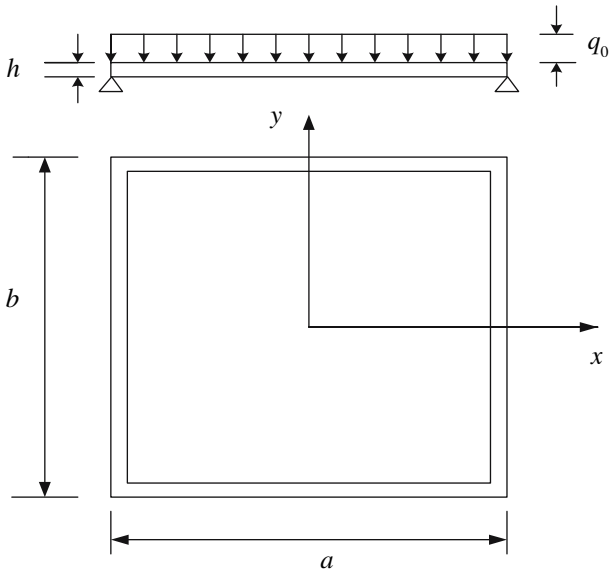

Fig. 4 A square plate subjected to uniform transverse load

Table 1 Transverse center displacement $\tilde{w} = wEh^3/q_0a^4$ of a square plate ($a = b = 10$ in., $\nu = 0.3$)

Simply supported ($a/h = 10$)		Clamped ($a/h = 100$)	
Nodes	$\tilde{w}$	Nodes	$\tilde{w}$
5×5	0.04759	7×7	0.01429
7×7	0.04674	9×9	0.01422
9×9	0.04653	11×11	0.01423
11×11	0.04650	13×13	0.01405
		15×15	0.01404

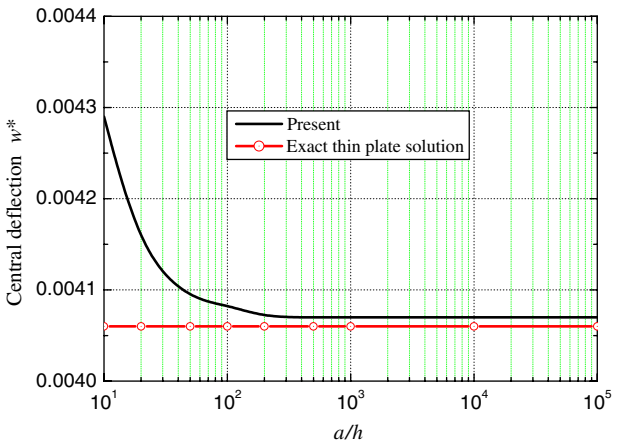

Fig. 5 Shear locking test for a simply supported square plate ($\nu = 0.3$)

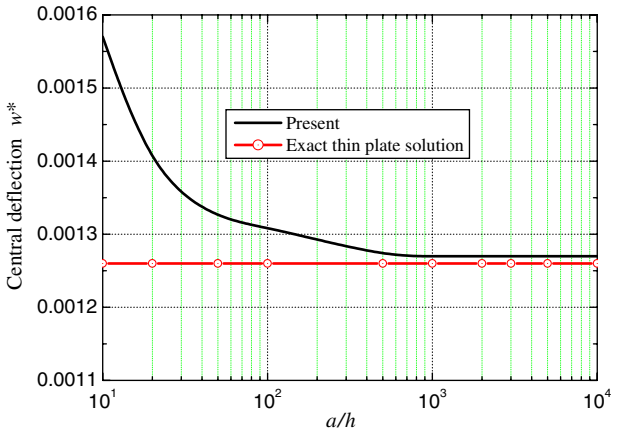

Fig. 6 Shear locking test for a clamped square plate ($\nu = 0.3$)

Figure 5 shows the locking test results for a simply supported square plate under uniform load. The deflection is normalized as $w^* = wEh^3/12(1-\nu^2)qa^4$. It is clearly seen that, as the plate becomes thinner, shear locking does not arise. A similar trend is also observed from Fig. 6 for a clamped square plate subjected to uniform load.

A pinched cylinder is supported at each end by rigid diaphragm and subjected to a pair of pinching loads $P = 1$, as shown in Fig. 7. This case has been studied by many researchers. The geometric properties of the cylinder are length $L = 600$ in, radius $R = 300$ in, and thickness $h = 3$ in. The material constants are Young's modulus $E = 3 \times 10^6$ and Poisson ratio $\nu = 0.3$. Due to the symmetry, an octant of the cylinder is modeled. The analytical solution of the deflection under the point load is 1.8248×10^{-5} in [28]. Table 2 shows the comparison of the present solution with those given by Reddy [12] and Flügge [28]. It is observed that the RPIM solution is closed to the FEM result [12], but slightly larger than the analytical solution. It is also seen that the convergence trend is monotonic.

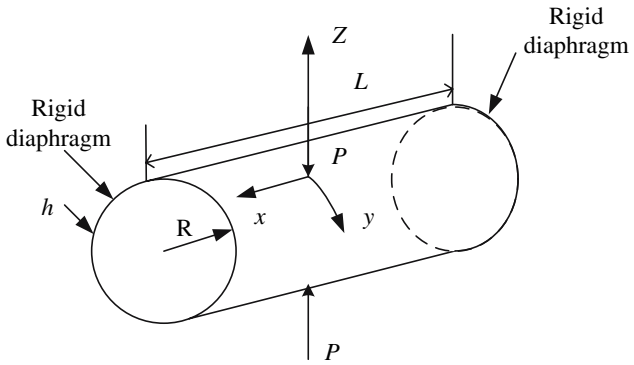

Fig. 7 Geometry of the pinched circular cylinder ($L = 600$ in., $R = 300$ in., $h = 3$ in., $E = 3 \times 10^6$, $\nu = 0.3$, $P = 1$)

Table 2 Transverse center displacement of a pinched cylindrical shell ($L = 600$ in, $R = 300$ in, $h = 3$ in, $E = 3 \times 10^6$psi, $\nu = 0.3$)

Present Nodes	$w(\times 10^{-5})$	Flügge [28] ($\times 10^{-5}$)	Reddy [12] ($\times 10^{-5}$)
15 × 15	1.6784	1.8248	1.8672
17 × 17	1.7213		
19 × 19	1.7991		
21 × 21	1.8327		
23 × 23	1.8596		
25 × 25	1.8663		

5.2 Nonlinear analysis of plates

5.2.1 Simply supported plates

A simply supported square plate subjected to a uniformly distributed load q_0 is considered (Fig. 4). This example was studied by Reddy [12] using finite element method. The side length and thickness of the square are $a = b = 10$ in and $h = 1$ in. The material properties for this isotropic plate are $E = 7.8 \times 10^6$ psi and $\nu = 0.3$. The nondimensional deflection and load are defined as $\bar{w} = w/h$ and $\bar{q} = q_0a^4/Eh^4$, respectively. A quarter of the plate is modeled due to the symmetry. Two types of simply supported boundary

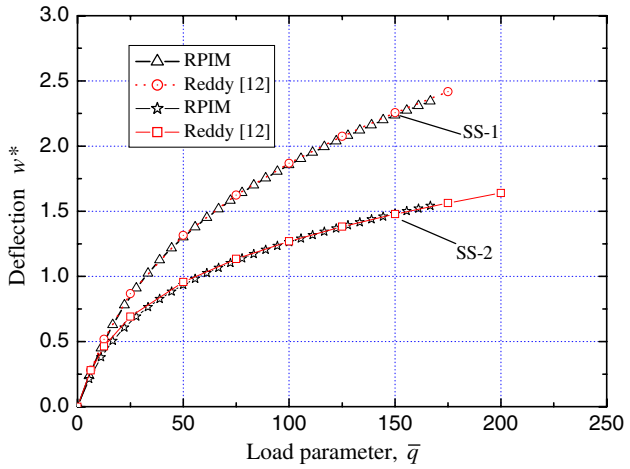

Fig. 8 Nonlinear center deflection parameter versus load parameter for simply supported, isotropic square plate under uniform load ($a = b = 10$ in., $h = 1$ in., $E = 7.8 \times 10^6$, $\nu = 0.3$)

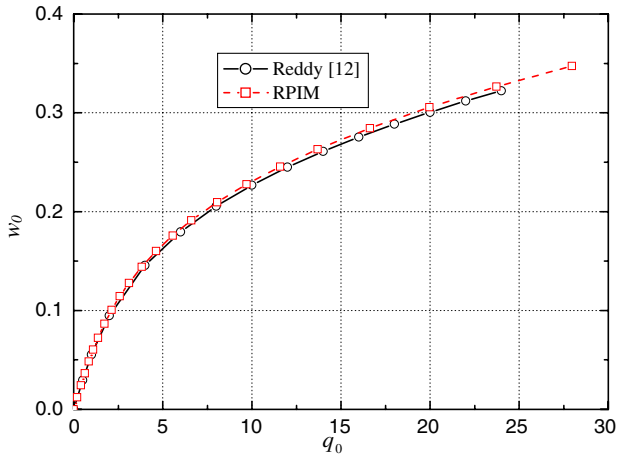

Fig. 9 Nonlinear center deflection versus load for a clamped, orthotropic square plate under uniform load ($a = b = 12$ in., $h = 0.138$ in., $E_1 = 3.0 \times 10^6$psi, $E_2 = 1.28 \times 10^6$psi, $\nu_{12} = 0.32$, $G_{12} = G_{13} = G_{23} = 0.37 \times 10^6$psi)

conditions are considered. The displacement boundary conditions termed SS-1 and SS-2 are given by

$$\begin{aligned} &\text{SS-1}: \quad \text{At } x = a/2 : v_0 = w_0 = \psi_y = 0 \\ &\qquad\quad \text{At } y = b/2 : u_0 = w_0 = \psi_x = 0 \end{aligned} \tag{66}$$

$$\text{SS-2}: \quad u_0 = v_0 = w_0 = 0, \quad \text{on all four edges} \tag{67}$$

The boundary conditions along the symmetry lines are expressed by

$$\text{At } x = 0 : \quad u_0 = \psi_x = 0; \quad \text{At } y = 0 : \quad v_0 = \psi_y = 0 \tag{68}$$

Figure 8 shows the load-displacement curves of central point for both cases. The solutions are obtained by using a 11×11 nodal distribution. It is observed that, for both cases, the center displacement increases with rising load, and the case associated with SS-2 produces lower transverse deflections than case with SS-1 due to more edge constraints in SS-2. The present RPIM method can be seen to give very satisfactory results in comparison to solutions reported by Reddy [12].

5.2.2 Clamped plates

A clamped, orthotropic plate under uniformly distributed transverse load q_0 is analyzed first. The geometric properties are: $a = b = 12$ in and $h = 0.138$ in. The material parameters are: $E_1 = 3 \times 10^6$ psi, $E_2 = 1.28 \times 10^6$ psi, $G_{12} = G_{13} = G_{23} = 0.37 \times 10^6$ psi, and $\upsilon_{12} = 0.32$. The clamped boundary conditions at all edges are taken to be

$$u_0 = v_0 = w_0 = \psi_x = \psi_y = 0 \tag{69}$$

A quarter of the plate is modeled because of the symmetry of the plate. A nodal distribution of 15×15 is used in this case. Figure 9 depicts the load-deflection responses obtained from RPIM and given by Reddy [12]. It is clearly seen that excellent agreement is attained.

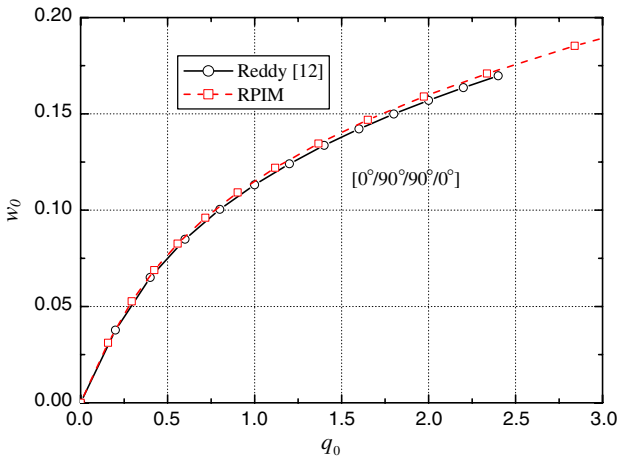

Fig. 10 Nonlinear center deflection versus load for a clamped, cross-ply ($0°/90°/90°/0°$) square plate under uniform load ($a = b = 12$ in., $h = 0.096$ in., $E_1 = 1.8282 \times 10^6$ psi, $E_2 = 1.8315 \times 10^6$ psi, $\nu_{12} = 0.24$, $G_{12} = G_{13} = G_{23} = 0.3125 \times 10^6$ psi)

A laminated composite plate with lamination sequence ($0°/90°/90°/0°$) is also studied. This symmetric cross-ply plate is clamped at all edges and the geometric and material properties are: $a = b = 12$ in., $h = 0.096$ in. (each layer of 0.024 in. thick), $E_1 = 1.8282 \times 10^6$ psi, $E_2 = 1.8315 \times 10^6$ psi, $G_{12} = G_{13} = G_{23} = 0.3125 \times 10^6$ psi and $\upsilon_{12} = 0.2395$. A total of 15×15 nodes is used. Figure 10 describes the load-deflection paths of center point of the composite plate. It can be observed that the present results compares well with solutions reported in the literature [12].

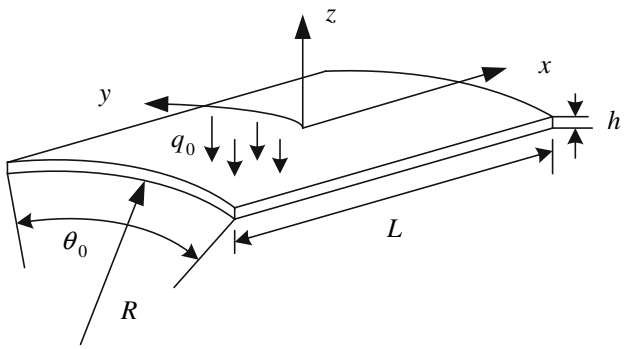

Fig. 11 Isotropic clamped cylindrical shell panel under uniform radial pressure q_0

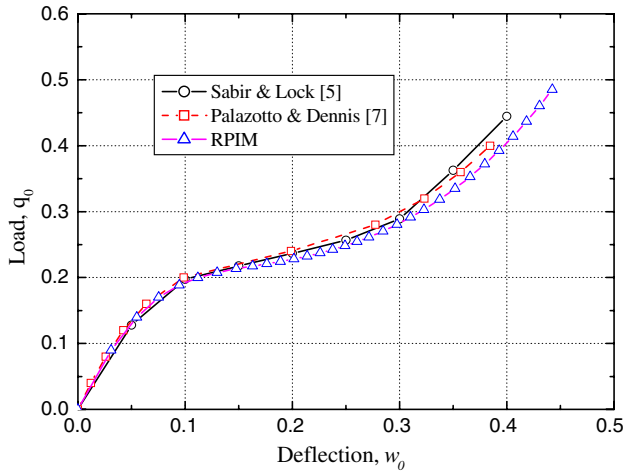

Fig. 12 Nonlinear response of a clamped cylindrical shell panel ($L = 20$ in., $R = 100$ in., $h = 0.125$ in., $\theta_0 = 0.2$ rad, $E = 4.5 \times 10^5$, $\nu = 0.3$)

5.3 Nonlinear analysis of shells

5.3.1 A clamped cylindrical panel

The nonlinear behavior of an isotropic clamped cylindrical shell panel under uniform transverse pressure, as shown in Fig. 11, is examined. The geometry parameters of the panel are: $L = 20$ in., $R = 100$ in., $h = 0.125$ in. and $\theta_0 = 0.2$ rad. The material properties are: $E = 4.5 \times 10^5$ psi and $\nu = 0.3$. The boundaries conditions are same with those given in Eq. (68). A quarter of the panel is modeled due to the symmetry. A regular grid nodes 15×15 is used. The RPIM results for the center deflection, together with solutions given by Sabir and lock [5] and Palazotto and Dennis [7], are plotted in Fig. 12. It can be seen, that the trends of three sets of solutions agree well for load up to 0.3 psi, although small disparities are observed for load more than 0.3 psi. The differences could be due to errors in reading the published graph, the difference in the shell formulations and the solution strategy.

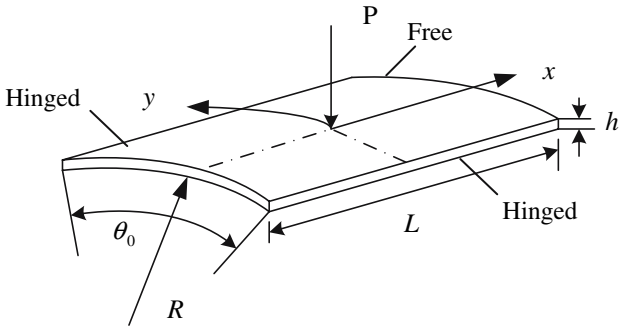

Fig. 13 Hinged cylindrical shell under point load

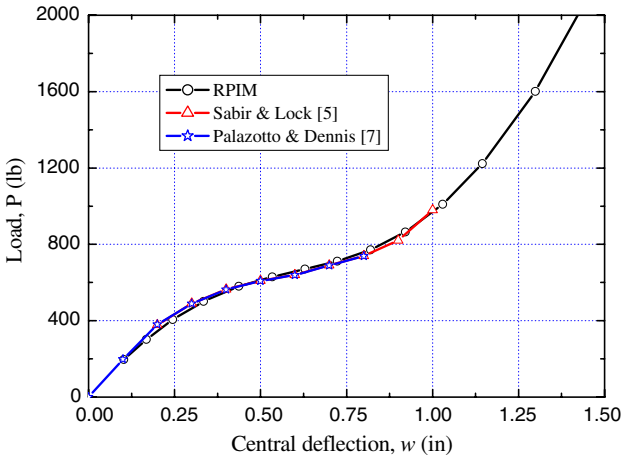

Fig. 14 Nonlinear response of point loaded cylindrical shell panel ($L = 20$ in., $h = 1.0$ in., $R = 100$ in., $\theta_0 = 0.2$ rad, $E = 4.5 \times 10^5$ psi, $\nu = 0.3$)

5.3.2 Hinged cylindrical shell under concentrated load

The hinged cylindrical shell subjected to a concentrated load, as shown in Fig. 13, is a typical test case for geometric nonlinear response analysis of shell panels. A quarter of the shell is modeled owing to symmetry. Panels with different thicknesses $h = 25.4$ mm ($h = 1.0$ in.), $h = 12.7$ mm ($h = 0.5$ in.) and $h = 6.35$ mm ($h = 0.25$ in.) are examined in this study. The other geometry parameters and material properties are same with those given in Sect. 5.3.1. The boundary conditions at the hinged edges are given by

$$u_0 = v_0 = w_0 = \psi_x = 0 \tag{70}$$

For the shell with thickness $h = 1.0$ in., a nodal distribution of 15×15 is adopted. Figure 14 shows the center point load-deflection responses of RPIM solutions and results given by Sabir and Lock [5], and Palazotto and Dennis [7]. It is seen that present PRIM solutions agree well with those reported in literature.

Figure 15 depicts the nonlinear response of a shell panel with thickness $h = 12.7$ mm. a regular node distribution of 17×17 is used. The results given by Sabir and Lock [5]

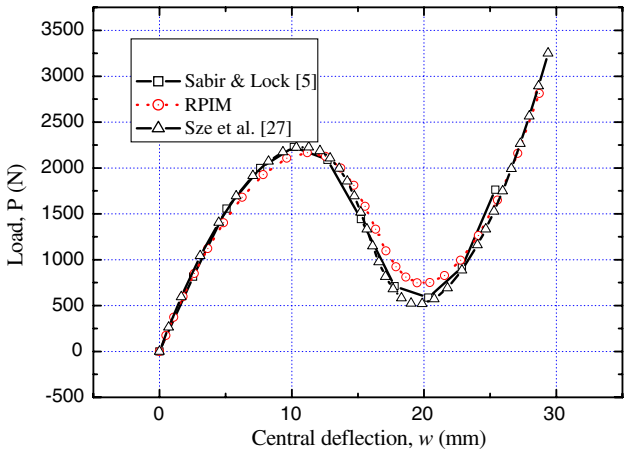

Fig. 15 Nonlinear response of point loaded cylindrical shell panel ($h = 12.7$ mm)

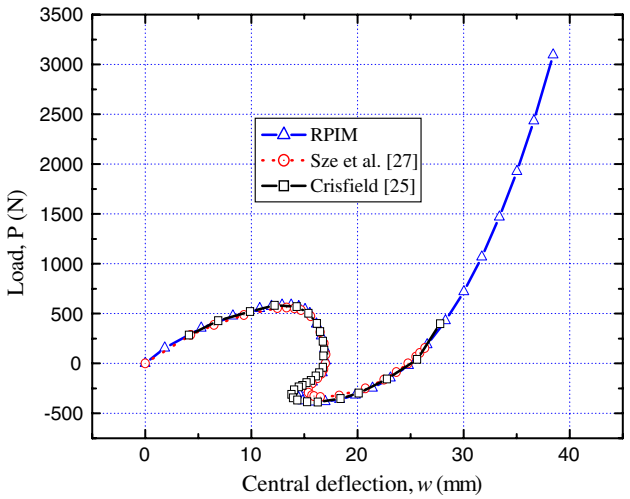

Fig. 16 Nonlinear response of point loaded cylindrical shell panel ($h = 6.35$ mm)

and Sze et al. [29] are also plotted in Fig. 12 for comparison purpose. A snap-through behavior is observed for this shell panel. It is seen that, in general, three curves agree well, except that the low limit point load calculated from RPIM is slightly higher than results reported in literature.

Figure 16 shows the load-deflection curves for a shell panel with thickness $h = 6.35$ mm. A total of 21×21 nodes is used. A snap-back phenomenon is noticed for this shell panel. The RPIM solutions are compared with results computed by Sze et al. [29] using ABACUS and Crisfield [25] using finite element method. It is clearly seen that the PRIM has successfully captured the negative load limit point, and the present results agree well with those given in literature.

Figure 17 shows the load-deflection responses of laminated shell panels subjected to point load. Two lamination sequences, $[90°/0°/90°]$ and $[0°/90°/0°]$, are considered in this study. The shell thickness is $h = 12.7$ mm. The mate-

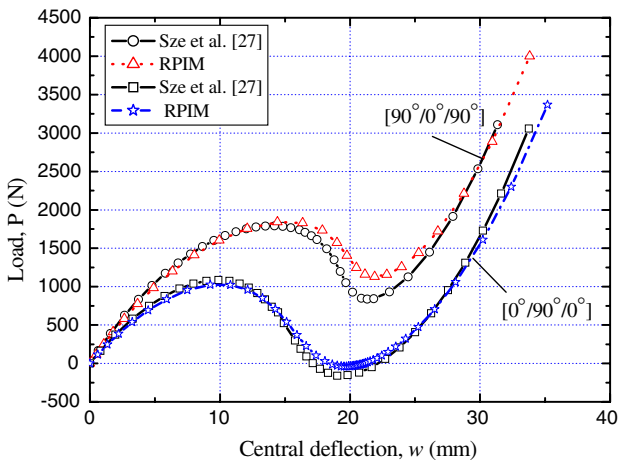

Fig. 17 Load-deflection responses of laminated cylindrical shell panels ($[0°/90°/0°]$, $[90°/0°/90°]$) under point load ($h = 12.7$ mm, $E_L = 3{,}300$, $E_T = 1{,}100$, $G_{LT} = 660$, $\nu_{LT} = \nu_{TL} = 0.25$)

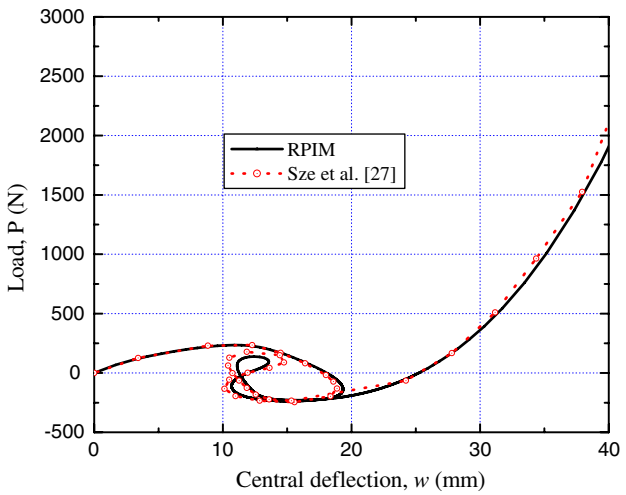

Fig. 18 Load deflection response of hinged cylindrical shell with lamination sequence $[0°/90°/0°]$ ($h = 6.35$ mm, $E_L = 3{,}300$, $E_T = 1{,}100$, $G_{LT} = 660$, $\nu_{LT} = \nu_{TL} = 0.25$)

rial properties are: $E_L = 3{,}300$, $E_T = 1{,}100$, $G_{LT} = 660$ and $\nu_{LT} = \nu_{TL} = 0.25$. A nodal distribution of 17×17 nodes is adopted. It can be concluded from the observation, that the lamination sequence has significant influence on the nonlinear behavior of shell panels. It is noticed that the values of loads at the lowest limits obtained from RPIM are higher than those given in literature for both cases. Figure 18 describes the nonlinear response of a laminated shell panel with lamination $[0°/90°/0°]$ and thickness $h = 6.35$ mm. A 19×19 nodal distribution is used. A complicated load-deflection relationship is observed and the present RPIM solutions compares well with results reported in literature [29]. It is concluded from these two examples, that both the lamination sequence and thickness play important roles in nonlinear responses of shells.

6 Conclusions

In this paper, the geometric nonlinear analysis of plates and shells are carried out by using a linearly conforming radial point interpolation method. Both the radial and polynomial basis functions are employed to construct the RPIM shape functions. A strain smoothing technique was introduced for the stabilization of nodal integration. The present formulations are validated by a variety of benchmark tests. Numerical examples have demonstrated that the present method provides very stable and accurate solutions for plate and shell analysis, and is able to capture the limit points in snap-through and snap-back phenomena in shells.

References

1. MacNeal RH, Harder RL (1985) A proposed standard set of problems to test finite element accuracy. Finite Elem Anal Des 1:3–20
2. Belytschko T, Stolarski H, Liu Wk, Carpenter N, Ong JSJ (1985) Stress projection for membrane and shear locking in shell finite elements. Comput Methods Appl Mech Eng 51:221–258
3. Simo J, Fox DD (1989) On a stress resultant geometrically exact shell model, part I: formulation and optimal parameterization. Comput Methods Appl Mech Eng 72:267–304
4. Simo J, Fox DD, Rifai MS (1989) On a stress resultant geometrically exact shell model, part II: the linear theory. Comput Methods Appl Mech Eng 73:53–92
5. Sabir AB, Lock AC (1973) The application of finite elements to the large deflection geometrically nonlinear behaviour of cylindrical shells. In: International conference on variational methods in engineering, Southampton, England, pp 7/67–7/76
6. Bergan PG, Nygard MK (1985) Nonlinear shell analysis using free formulation finite elements. In: Finite element methods for nonlinear problems, Europe–US Symposium, Tronhelm, Norway
7. Palazotto AN, Dennis ST (1992) Nonlinear analysis of shell structures. AIAA education series, Wahsington DC
8. Choi CK, Paik JG (1996) An effective four node degenerated shell element for geometrically nonlinear analysis. Thin-Walled Struct 24:261–283
9. Sze KY, Zheng SJ (1999) A hybrid-stress nine-node degenerated shell element for geometrical nonlinear analysis. Comput Mech 23:448–456
10. Sze KY, Chan WK, Pian THH (2002) An eight-node hybrid-stress solid-shell element for geometric nonlinear analysis of elastic shells. Int J Numer Methods Eng 55:853–878
11. Hauptmann R, Schweizerhof K (1998) A systematic development of solid-shell element formulations for linear and nonlinear analyses employing only displacement degrees of freedom. Int J Numer Methods Eng 42:49–69
12. Reddy JN (2004) Mechanics of laminated composite plates and shells: theory and analysis, 2nd edn. CRC Press, Baca Raton
13. Arciniega RA, Reddy JN (2007) Large deformation analysis of functionally graded shells. Int J Solids Struct 44:2036–2052
14. Krysl P, Belytschko T (1996) Analysis of thin shells by the element-free Galerkin method. Int J Solids Struct 33:3057–3080
15. Noguchi H, Kawashima T, Miyamura T (2000) Element free analyses of shell and spatial structures. Int J Numer Methods Eng 47:1215–1240
16. Li S, Hao W, Liu WK (2000) Numerical simulations of large deformation of thin shell structures using meshfree methods. Comput Mech 25:102–116
17. Wang JG, Liu GR (2002) A point interpolation meshless method based on radial basis functions. Int J Numer Methods Eng 54:1623–1648
18. Liu GR, Gu YT (2001) A point interpolation method for two-dimensional solids. Int J Numer Methods Eng 50:937–951
19. Liu GR, Dai KY, Lim KM, Gu YT (2003) A radial point interpolation method for simulation of two-dimensional piezoelectric structures. Smart Mater Struct 12:171–180
20. Zhang GY, Liu GR, Wang YY, Huang HT, Zhong ZH, Li GY, Han X (2007) A linearly conforming point interpolation method (LC-PIM) for three-dimensional elasticity problems. Int J Numer Methods Eng 72:1524–1543
21. Liu GR, Li Y, Dai KY, Luan MT, Xue W (2006) A linearly conforming RPIM for solids mechanics problems. Int J Comput Methods 3:401–428
22. Beissel S, Belytschko T (1996) Nodal integration of the element-free Galerkin method. Comput Methods Appl Mech Eng 139:49–74
23. Bonet J, Kulasegaram S (1999) Correction and stabilization of smoothed particle hydrodynamics methods with applications in metal forming simulations. Int J Numer Methods Eng 47:1189–1214
24. Chen JS, Wu CT, Yoon S, You Y (2001) A stabilized conforming nodal integration for Galerkin mesh-free methods. Int J Numer Methods Eng 50:435–466
25. Crisfield MA (1997) Non-linear finite element analysis of solids and structures, vol 2. Wiley, Chichester
26. Sze KY, Chen JS, Sheng N, Liu XH (2004) Stabilized conforming nodal integration: exactness and variational justification. Fin Elem Anal Des 41:147–171
27. Sanders JL Jr (1963) Nonlinear theories for thin shells. Q Appl Math 21:21–36
28. Flügge W (1973) Stresses in shells, 2nd edn. Springer, Berlin
29. Sze KY, Liu XH, Lo SH (2004) Popular benchmark problems for geometric nonlinear analysis of shells. Fin Elem Anal Des 40:1551–1569